Firehose Driven Magnetic Fluctuations in the Magnetosphere

W. Horton B.-Y. Xu, and H. Vernon Wong

Institute for Fusion Studies, The University of Texas at Austin, Austin, TX 78712 USA

The nonlinear saturation of the firehose instability in the high plasma pressure central plasma sheet is shown to produce a wide spectrum of Alfvénic fluctuations in the range of Pi-2 geomagnetic pulsations. The wave energy sources are the small $p_\parallel/p_\perp > 1 + B^2/\mu_0 p_\perp$ anisotropies which are created by Earthward ion convection at constant first and second adiabatic invariants. In the nonlinear state, the field-line curvature force is weaker than the linear force. This weakening of the driving force limits the amplitude of the Alfvénic fluctuations. Away from the equatorial plane, the plasma is firehose stable, but carries large magnetic fluctuations.

1. Introduction

Geomagnetic pulsations of the Pi-2 type are defined as magnetic fluctuations with periods in the range 40-200s with irregular wave forms. The geomagnetic Pi-2 oscillations are known to be intimately correlated with substorm growth and onsets [*Sigsbee et al., 2002*] and bursty bulk flows [*Kepko and Kivelson, 2001*].

During the time of enhanced Earthward plasma convection, there are numerous nonequilibrium features that develop in the ion phase space density distributions, including currents and anisotropies, that may serve to trigger low and ultra-low frequency instabilities. Here we argue that ion pressure anisotropies $p_\parallel > p_\perp$ associated with convection or bursty bulk flows drive nonlinear Pi-2 type fluctuations in the geomagnetic tail. We find that the nonlinear firehose driven fluctuations have a rich $k_\parallel\omega$-spectrum and that the local nonlinear firehose stability parameter

$$\sigma(t) = 1 - \frac{\mu_0(p_\parallel - p_\perp)}{[B^2 + \delta B_\perp^2(t)]} \tag{1}$$

fluctuates with only short-lived excursions into the unstable domain $\sigma(t) < 0$ occurring at the equatorial plane where the curvature $\boldsymbol{\kappa} = (\boldsymbol{b}\cdot\nabla)\boldsymbol{b}$ vector has its maximum value.

Kaufmann et al. [2000] use one year of one-minute Geotail data to analyze the firehose parameter $A = \mu_0(p_\parallel - p_\perp)/B^2$ as a function of β. *Kaufmann et al.* [2000] report A ranging from -0.1 to $+0.4$ with the values closer to zero occurring in the high-β bins. The number of data samples in the high-beta bins, $\beta > 30$ and $10 < \beta < 30$, is, however, low. *Kaufmann et al.* [2000] conclude that while A from the data is a few tenths, that the methodology used underestimates the value of A.

Chen and Wolf [1999] develop a model for bursty bulk flows that follows an Earthward accelerated flux tube that develops a firehose instability due to the faster increase of $p_\parallel$ from the shortening of the magnetic field line lengths than of $p_\perp$ from B. *Ji and Wolf* [2002] follow up the Chen and Wolf model with a detailed Lagrangian simulation model that couples the firehose dynamics to the magnetoacoustic wave dynamics. They find a shock front propagating to the Earth and the development of the firehose instability at the largest $k_\parallel = \pi/\Delta$ in the simulation. They pose the problem of finding the kinetic theory physics that limits the $|k_\parallel|$ for the growth rate and finding the nonlinear saturation level.

0094-8276/03/$5.00

2. Nonlinear Firehose Model

In this letter we present a kinetically-modified Eulerian ion fluid description of the nonlinear firehose instability for the magnetotail problem. We use a simple field-line model with an anisotropic pressure.

At latitude θ, the $\sigma(t,\theta) \to 1$ with the fluctuation energy $w_B = (\delta B_x^2/2\mu_0)$ and $w_K = \frac{1}{2}\rho(E_y^2/B^2)$ flowing into the region from the magnetic equatorial plane. Outside the high plasma pressure region $\beta = 2\mu_0\, p_\perp/B^2 \gg 1$ the oscillations are large amplitude Alfvén waves at finite $k_\parallel\rho_i$ where $\rho_i = (m_i T_i)^{1/2}/eB$ is the ion gyroradius. The finite ion gyroradius effects and the finite ion inertial scale c/ω_{pi} effects determine the maximum growth rate $\gamma_{\max} = \max_{k_z}[\gamma(k_z)]$ of the firehose instability. The calculation of these dispersion terms is well known and gives rise to the following linear dispersion relation

$$\frac{\omega^2}{\omega_{ci}^2} - \frac{\omega}{\omega_{ci}}\frac{k_\parallel^2 T_\parallel}{m_i\omega_{ci}^2} + \frac{k_\parallel^2(T_\parallel - T_\perp)}{m_i\omega_{ci}^2} - \frac{k_\parallel^2 c^2}{\omega_{pi}^2} = 0 \tag{2}$$

where we neglect the Landau damping contributions from the warm plasma kinetic dispersion relation [*Stix, 1992, Gary, 1993*]. For $k_\parallel\rho_i = (k_\parallel\, c/\omega_{pi})(\beta_i/2)^{1/2} \ll 1$ the linear dispersion term in ω/ω_{ci} is negligible and Eq. (2) yields the MHD firehose instability $\omega^2 = k_\parallel^2 v_A^2\sigma$ with σ defined in Eq. (1). For $p_\parallel/p_\perp > 1 + 2/\beta_i$ the MHD growth rate is $\gamma_{k_\parallel} = |k_\parallel| v_A\sqrt{-\sigma}$ increasing monotonically with $k_\parallel$. From the kinetic dispersion relation there is a well-defined maximum growth rate at $k_\parallel\rho_i = \sqrt{2}(1 - T_\perp/T_\parallel - 2/\beta_{i\parallel})^{1/2}$ where the maximum growth rate

$$\gamma_{\max} = \omega_{ci}(1 - T_\perp/T_\parallel - 2/\beta_{i\parallel}). \tag{3}$$

We have written an initial value code using the dipole magnetic field lines and typically taking the mass density $\rho(s) \propto B(s)$ to study the linear and nonlinear kinetically-modified Alfvénic-Firehose turbulence occurring in the night-side magnetotail. The nonlinear equation for the complex displacement field $\xi(z,t)$ is

$$\frac{\partial^2\xi}{\partial t^2} = v_A^2\frac{\partial}{\partial z}\sigma_{n\ell}\frac{\partial\xi}{\partial z} + i\nu\,\frac{\partial^3\xi}{\partial t\partial z^2} \tag{4}$$

where $\sigma_{n\ell}$ is given in Eq. (1) with $B^2 = B_n^2\left(1 + |\partial_z\xi|^2\right)$ and $\nu = \omega_{ci}\rho_i^2 = cT_{i\parallel}/eB$ follows from Eq. (2). The complex valued fields are $\xi = \xi_x + i\xi_y$ and $\delta B/B_n = \partial_z\xi_x + i\partial_z\xi_y$ with the real $\delta B^2 = B_n^2 + \delta B^*\delta B$ used in Eq. (1). The last term in Eq. (4) describes the Faraday rotation of the polarization vector of the Alfvén wave. The phase rotation $\delta\phi$ in time Δt is $\delta\phi = \nu k_\parallel^2\Delta t = k_\parallel^2(cT_{i\parallel}/eB)\Delta t$.

The derivation of Eq. (4) follows from the acceleration equation

$$\rho\frac{dv_x}{dt} = F_x^{n\ell} = j_y B_z - \widehat{\boldsymbol{e}}_x\cdot\nabla\cdot\boldsymbol{P} \tag{5}$$

where $\boldsymbol{P} = (p_\parallel - p_\perp)(\boldsymbol{BB}/B^2) + p_\perp \boldsymbol{I}$, $\boldsymbol{B} = B_n\widehat{\boldsymbol{e}}_x + \delta B_x\widehat{\boldsymbol{e}}_x$, $j_y = \frac{1}{\mu_0}\frac{\partial B_x}{\partial z} = \frac{B_n}{\mu_0}\frac{\partial^2\xi}{\partial z^2}$ and $\delta B_x = B_z\partial_z\xi$ from Faraday's law $\partial_z E_y = \partial B_x/\partial t$ and Ohm's law $E_y - v_x B_z = E_y - B_z(\partial\xi/\partial t) = 0$. The inertial acceleration from the $j_y B_z$ force gives $\partial_t^2\xi = v_A^2\partial_z^2\xi$. The nonlinear pressure gradient force follows from the calculation of

$$\widehat{\boldsymbol{e}}_x\cdot\nabla\cdot\boldsymbol{P} = (p_\parallel - p_\perp)\left[\widehat{\boldsymbol{e}}_x\cdot(\widehat{\boldsymbol{b}}\cdot\nabla)\widehat{\boldsymbol{b}} + b_x\nabla\cdot\widehat{\boldsymbol{b}}\right] \tag{6}$$

which reduces to

$$(p_\parallel - p_\perp)B_z\frac{\partial}{\partial z}\left(\frac{B_z}{B^2}\frac{\partial\xi}{\partial z}\right) \tag{7}$$

after using $B = B_n(1+|\partial_z\xi|^2)^{1/2}$ and $B_n = B_z = $ constant.

The nonlinear driving term $F_x^{n\ell}$ at small $\delta B_x/B = \partial_z\xi \ll 1$ is proportional to the field-line displacement ξ. At large amplitudes $\delta B_x/B \lesssim 1$ the force is greatly weakened, eventually decreasing with ξ as $\partial_z^2\xi/|\partial_z\xi|^2$. The effect is familiar as the decrease of curvature for a string $y = y(x)$ given by the curvature formula $y''/(1+y'^2)^{3/2}$. This may be called the magnetic field line crinkling.

The nonlinear partial differential equation (4) develops mode coupling from the nonlinear curvature force. The nonlinear partial differential equation for $U(\widehat{\boldsymbol{z}},\tau) = B_z\xi(z/L, tv_{A0}/L)$ with $\tau = tB_z/(\mu_0\rho_0)^{1/2}L$ where L is the scale length ($\sim R_E$) of the field line variation is

$$\frac{\partial^2 U}{\partial\tau^2} - i\nu\frac{\partial^3 U}{\partial\tau\partial z^2} - \frac{\partial^2 U}{\partial z^2} + \frac{\mu_0(p_\parallel - p_\perp)}{B_z^2}\frac{\partial}{\partial z}\left(\frac{1}{1+|\frac{\partial U}{\partial z}|^2}\frac{\partial U}{\partial z}\right) = 0 \tag{8}$$

with boundary conditions $U(z = \pm L,\tau) = 0$. Here $\nu = T_{\parallel i}/eBLv_{A0} = \rho_{ix}v_{\parallel i}/Lv_A$.

The total energy is

$$W_T(t) = K(t) + W_B + W_P(t) \tag{9}$$

where $K = \int_{-\theta_0}^{\theta_0} d\theta\,\frac{1}{2}\rho(\partial\boldsymbol{\xi}/\partial t)^2$, $W_B = \int_{-\theta_0}^{\theta_0} d\theta\,\delta\boldsymbol{B}^2/2\mu_0$ and $W_P = -A/2\int_{-\theta_0}^{\theta_0}\frac{B_z^2}{\mu_0}\ell n\left[1+\left(\left|\frac{\partial\xi}{\partial z}\right|\right)^2\right]d\theta$. We use the energy invariant to test the accuracy of the numerical solutions.

The nonlinear potential is of the type that occurs in the derivative nonlinear Schrödinger equation (DNLS) which governs dispersive Alfvén waves [*Horton and Ichikawa, 1996*]. In perturbative theory the nonlinear force weakens as $F_x^{n\ell} \simeq \frac{B_n^2}{2\mu_0}[A - 1 - A|\partial_z\xi|^2](\partial_z^2\xi)$. Here we show a typical example of the solution of Eq. (8). In a future work, we will develop solutions for the magnetotail that include parametric decays of these fluctuations into Alfvén waves and acoustic waves. A single $k_\parallel$-mode calculation shows that the saturated amplitude varies as $\xi_{\max} = k_\parallel^{-1}(A^{1/2}-1)^{1/2}$ and has the nonlinear frequency $\omega_A(A-1)^{1/2}$.

In addition to the intrinsic nonlinear force derived in Eq. (8) that saturates the instability and produces the nonlinear oscillations shown in Figs. 1-4, there is the quasilinear change of the pressure anisotropy due to reaction of the magnetic fluctuations on the background ion phase space distribution function [*Gary, 1993, and Sagdeev and Galeev, 1967*]. Here we ignore the quasilinear change of the pressures arguing that on the background evolution time scale there are processes building up the anisotropy competing with the quasilinear relaxation of the anisotropy. Thus, the turbulence shown here for a fixed value of $A = \mu_0(p_\parallel - p_\perp)/B_n^2$ given here overestimates the amplitude obtained with addition of the quasilinear background transport. In the simulation we model this effect rather crudely by setting $p_\parallel = p_\perp$ after some number of nonlinear oscillations. There follows a period of large amplitude Alfvén wave oscillations which may be subject to parametric instabilities for A above a critical value.

The simulations are performed as an initial value problem with equatorial field-line crossing at $x \sim 8R_E$ with $\beta_\perp(0) = 2\mu_0 p_\perp/B_n^2 = 5$ and $p_\parallel/p_\perp = 1.44$ so that $A = 1.1$ or $\sigma(t=0) = -0.1$ and $\nu = 0.01$. We use a 4th-5th over adaptive RK integrator to advance the finite differential equations on 129 grid points along the magnetic field line. The local equatorial field strength is $B_n \simeq 100\,$nT. The local ion gyroradius $\rho_i \cong 200\,$km.

3. Simulation Results

Figure 1a shows the fastest growing eigenfunction at $10t_A \simeq 820\,$s as a function position along the field line. Figure 1b shows that there is a well-defined eigenmode frequency ($\omega = 2\pi f \sim 8/t_A \sim 5-10\,$mHz), Fig. 1c shows the spectrum of $k_\parallel = 2\pi n/L_\parallel$ values in the eigenmode. Figure 1d gives the profile of $\sigma(\theta, t = 10t_A)$. We have not calculated analytically the eigenmodes. The local equatorial plane frequency and growth rate for the most unstable $k_\parallel$ are $\omega \simeq \gamma_{\max} = 10(v_{A0}/L)$, but the observed eigenmode growth rate is much smaller than $\gamma_{\max}$ due to the localization of $\sigma(\theta)$.

Figure 2a and b show the magnetic fluctuations $\delta B_x(t)$ and its frequency spectrum $\delta B_x^2(\omega)$. Figure 2c gives the electric field fluctuations $E_y(t)$. Figure 2d shows the nonlinear state of the plasma defined by $\xi(t) = \xi_x(t) + i\xi_y(t)$ for a time interval $\Delta t = 15t_A \simeq 20\,$min in the saturated state. There are several characteristic frequencies in the dynamics. In this example, there is a short period signal $T_1 \simeq 100\,$s and a long nonlinear period $T_0 \simeq 300\,$s.

The time series in Fig. 2 for the electric and magnetic fields show a chaotic structure even though the power is concentrated in two frequencies. Such spectra are typical of lower-order dynamical systems suggesting a search for a low-order model derived from the pde. There are bursts of energy releases from the nonlinear dynamics that are one aspect of a self-organized criticality (SOC) system. The second aspect of space-scale invariance of an SOC system is not satisfied due to the key role of the ion gyroradius in defining the fast-growing linear mode at $k_{\parallel,\max}$. The turbulent fluctuations mode-couple to both shorter and longer wavelength fluctuations. For $\sigma = 1$ there are soliton solutions to the associated DNLS equation [*Horton and Ichikawa, 1996*] derived by factoring the Alfvén equation into uncoupled right and left propagating waves. In the present problem the driving by the pressure anisotropy disrupts those solitons and couples the parallel (right) and antiparallel (left) propagating Alfvén waves. For Eq. (8) we find coherent, localized solutions not unlike solitons for $\nu = 0.03$.

Figure 3 shows the three energy components in Eq. (9) for the solutions in Fig. 2. After the exponential growth the turbulence saturates with the magnetic fluctuation energy $W_B \simeq -W_P$ the source of instability and both large compared with kinetic energy K. In the simulation the total energy is well conserved as follows analytically from the model. Thus, there is an efficient conversion from the anisotropy thermal energy reservoir into magnetic energy. The increase of the magnetic turbulence with the anisotropy parameter A is shown in Fig. 4. At small $A-1$ values the system shows coherent structures and the error bars may underestimate the actual error.

4. Conclusions

In conclusion, the presence of small fractional pressure anisotropies in the high-beta magnetotail plasma produce an intermittent spectrum of Alfvénic fluctuations that are in the range of the Pi-2 signals commonly associated with bursty bulk flows [*Kepko and Kivelson, 1999 and 2001*] and substorm dynamics. The kinetic ballooning pressure gradient instability [*Roux et al., 1991*] remains a possible cause of these fluctuations. The nonlinear firehose model also produces candidate magnetic fluctuations and requires the kinetic dispersion term to give the maximum growth rate, the wave dispersion and polarization. The nonlinear model is integrated and shows irregular wave forms with intermittent turbulent energy releases. Further research that includes the driving sources of the anisotropy and the quasilinear velocity scattering of the ions from the magnetic fluctuations is required for a more detailed picture of the long-time evolution of the system.

In a related work [*Ji and Wolf, 2003b*] argue that the appearance of the anisotropy is a product of the near-Earth neutral line formation. Consequently, the observations of Pi-2 turbulence described here along the auroral field lines may be a signature of the flow braking from fast Earthward flows produced by a near-Earth neutral line. It remains for future 2D theory and simulations to find the balance of the quasilinear reduction of the anisotropy and its production by Earthward flows.

Finally, the problem of correlating the observed Pi2 oscillations with the various theoretical models remains.

Acknowledgments. The authors thank Richard Wolf and Shuo Ji for numerous useful discussions along the path to this solution. The work was supported by the National Science Foundation ATM-0229863.

References

Chen, C. X., and Wolf, R. A., Interpretation of high-speed flows in the plasma sheet. *J. Geophys. Res., 98*, 21409, 1993.

Chen, C. X., and R. A. Wolf, Theory of thin-filament motion in Earth's magnetotail and its application to bursty bulk flows, *J. Geophys. Res., 104*, 14613, 1999.

Gary, S. Peter, *Theory of Space Plasma Microinstabilities*, p. 127, Cambridge Univ. Press., 1993.

Horton, W., and Y.-H. Ichikawa, *Chaos and Structures in Nonlinear Plasmas*, pp. 221-273, chap. 6, World Scientific, 1996.

Ji, S., and R. A. Wolf, Double-adiabatic-MHD theory for motion of a thin magnetic filament and possible implications for bursty bulk flows, *J. Geophys. Res., 108*(A5), 10.1029/2002JA009655, 2003.

Ji, S., and R. A. Wolf, Firehose instability near substorm expansion onset, *J. Geophys. Res.*, accepted 2003b.

Kaufmann, R. L., B. M. Ball, W. R. Paterson, and L. A. Frank, "Pressure Anisotropy and B_y in the Magnetotail Current Sheet," in *Geophys. Monograph, 118*, pp. 323-330, Copyright 2000 by the American Geophysical Union.

Kepko, L., and M. G. Kivelson, Flow bursts, braking, and Pi2 pulsations, *J. Geophys. Res., 106*, 1903-1915, 2001.

Kepko, L., and M. G. Kivelson, Generation of Pi2 pulsations and bursty bulk flows, *J. Geophys. Res., 104*, 25, 021-25,034, 1999.

Roux, A., S. Perrault, P. Robert, A. Morane, A. Pedersen, A. Korth, G. Kremser, B. Aparicio, D. Rodgers, and R. Pellinen, Plasma sheet instability related to the westward traveling surge, *J. Geophys. Res., 96*, 17,697, 1991.

Sagdeev, R. Z., and Galeev A.A., and, *Nonlinear Plasma Theory*, Revised and edited by T. M. O'Neil and D. L. Book, pp. 67-73, W. A. Benjamin, Inc., New York, 1967.

Sigsbee, K., C. A. Cattell, D. Fairfield, K. Tsuruda, and S. Kokubun, Geotail observations of low-frequency waves and high-speed earthward flows during substorm onsets in the near magnetotail from 10 to 13 Re, *J. Geophys. Res., 107*, A7, 27, 2002.

Stix, T. H., *Waves in Plasmas*, pp. 383-436, American Institute of Physics, 1992.

W. Horton B.-Y. Xu, and H. Vernon Wong, Institute for Fusion Studies, The University of Texas at Austin, Austin, TX 78712 USA (e-mail: horton@physics.utexas.edu)

FIG. 1. (a) Fastest growing eigenfunction (solid line real part, dashed imaginary part) for $A = 1.1$ and $\beta_\perp(0) = 5$, (b) the eigenfrequency (solid line) and growth rate (dashed line) in units of v_{A0}/R_0 where v_{A0} and R_0 are the equatorial Alfvén speed and mirror field scale length, (c) the $k_\parallel$-spectrum of the eigenmode and (d) the initial profile of $\sigma(\theta)$ in Eq. (1).

FIG. 2. One-hour interval of steady-state turbulence driven by fixed $p_\parallel/p_\perp = 1.44$. (a) The magnetic fluctuations $\delta B_x(t)$, (b) the magnetic power spectrum $|\delta B_x(\omega)|^2$. (c) the electric field fluctuation $E_y(t)$ and (d) the displacement field $\xi = \xi_x + i\xi_y$ fluctuations (ξ_x solid, ξ_y dashed).

FIG. 3 The three energy components in Eq. (9) for the solution shown in Fig. 2. The total energy $W_{\rm total} = W_{\rm total}(t = 0) = 10^{-30}$.

FIG. 4 The increase of the mean value of the magnetic fluctuation energy W_B as a function of the anisotropy parameter A for fixed $\nu = 0.01$. The small error bars at low W_B are due to the small oscillations of $W_B(t)$ about the mean value. The actual errors are larger.

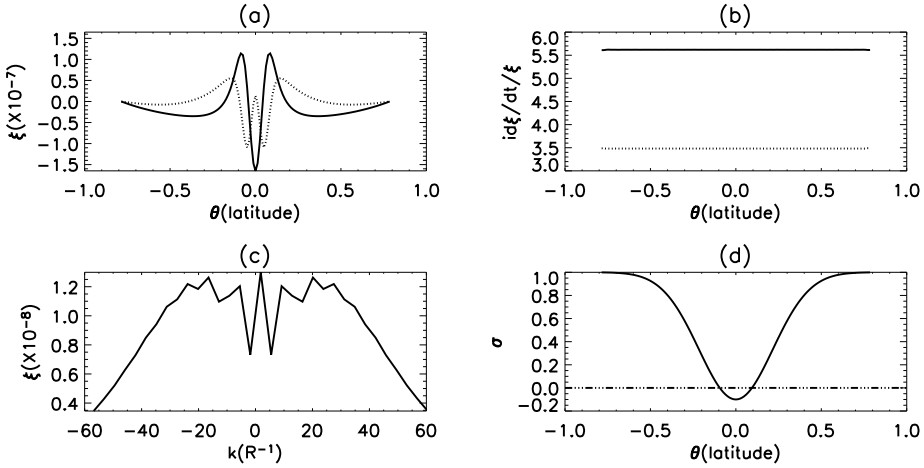

Figure 1.

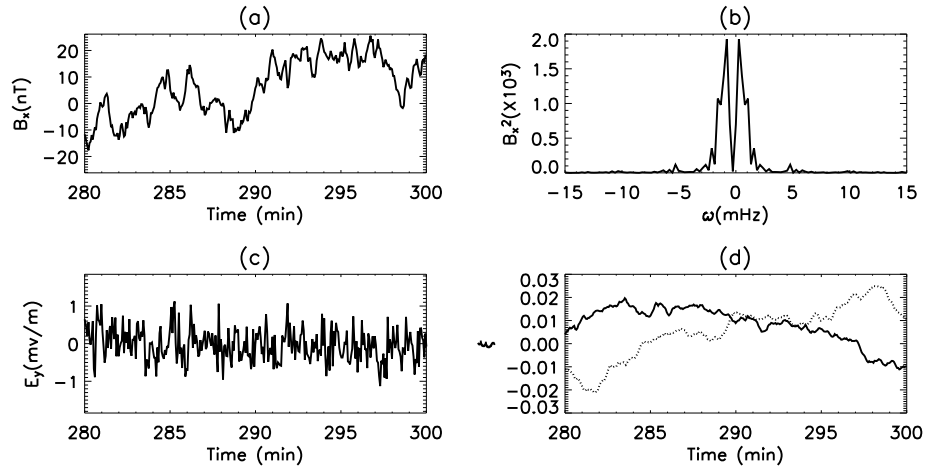

Figure 2.

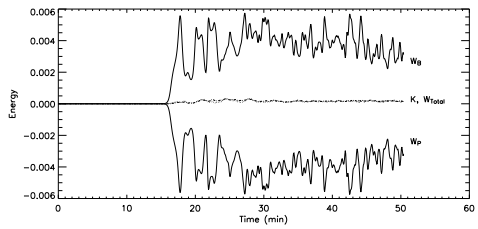

Figure 3.

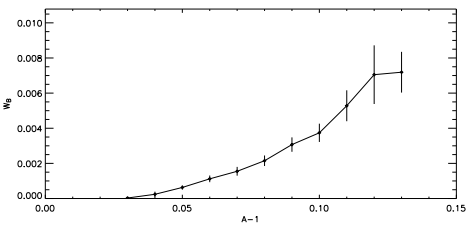

Figure 4.